ACS Energy LETTERS

Open Access

http://pubs.acs.org/journal/aelccp

Letter

Lattice-Vacancy-Mediated Structural Ordering of Pt-Based Alloy Nanocatalysts for Durable PEM Fuel Cell Cathodes

Jiasheng Lu, Carlos A. Campos-Roldán, Thomas Merzdorf, Xingli Wang, Lujin Pan, Hong Nhan Nong, Frederik Firschke, Sören Selve, Jakub Drnec, Deborah Jones, Fabio Dionigi, and Peter Strasser*

Cite This: ACS Energy Lett. 2026, 11, 3642−3650

Read Online

ACCESS | Metrics & More | Article Recommendations | Supporting Information

ABSTRACT: Atomically ordered Pt-based intermetallic alloys have gained interest as promising cathode materials catalyzing the oxygen reduction reaction (ORR) in hydrogen-fueled proton exchange membrane fuel cells (PEMFCs) with special durability requirements. This is the case because ordered Pt intermetallic alloys are believed to display superior chemical durability over their disordered counterparts. However, achieving the atomic-disorder-to-order phase transition typically necessitates prolonged high-temperature annealing, which often induces nanoparticle sintering and reduces Pt utilization. These challenges are particularly pronounced in acid-stable early transition metal Pt−M alloy systems (e.g., Pt−V), where alloy formation is hindered by the large disparity in reduction potentials. Here we present a lattice-vacancy-mediated synthesis strategy using evaporating Zn atoms as a *cataloreactant* to trigger the formation of the $L1_2$ intermetallic phase in the Pt−V system. This approach enabled the synthesis of highly ordered Pt−V alloy nanocatalysts with significantly suppressed non-noble transition metal leaching, thereby delivering enhanced PEMFC performance and durability. Online spectrometric and *in situ* spectroscopic analyses suggest distinct degradation mechanisms, characterized by *isotropic* V leaching in the ordered structure versus *anisotropic* segregation in the disordered structure. These findings underscore the efficacy of vacancy-mediated ordering as a synthetic paradigm for designing durable, high-performance intermetallic catalysts for PEMFC applications.

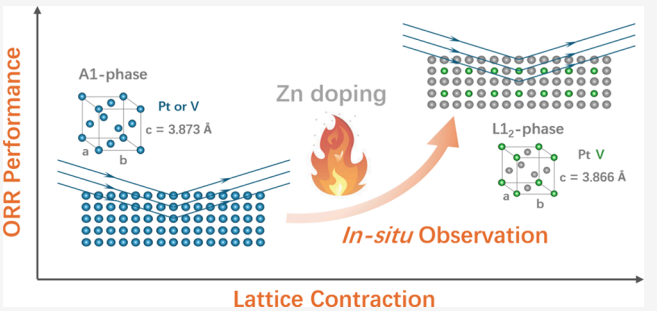

The hydrogen economy is increasingly recognized as a promising pathway toward a sustainable, low-carbon energy future. Proton exchange membrane fuel cells (PEMFCs) have shown promising potential in terms of efficiency and scalability among various hydrogen-based technologies.[1−3] In recent years, the increasing interest in heavy-duty-vehicle (HDV) PEMFC applications, however, urged researchers to address the giant challenge to boost both the durability and power density of PEMFCs compared to the state-of-the-art devices for light-duty-vehicles (LDVs). This HDV-fuel cell design challenge necessitates the development of thinner cathode catalyst layers with high weight loadings of at least 50 wt % Pt to ensure sufficient mass and charge transport.[4] This challenge also calls for the development of novel intermetallic Pt-based cathode catalysts that offer improved chemical stability and enhanced catalytic oxygen reduction reaction (ORR) activity due to their atomically ordered lattice structures.[5−9] To date, most research has focused on conventional intermetallic Pt−M alloy systems such as PtCo, PtNi, PtFe, and PtCu, which continue to suffer from severe dissolution of the less-noble metal under the harsh acidic conditions (pH < 1) during PEMFC operation.[10−17] A specific element doping (e.g., Cr, Sn, Ga) strategy for the PtCo, PtNi, and PtFe systems has been reported to tailor the lattice constant and further regulate the electron density surrounding the Pt atoms, leading to enhanced electrochemical stability.[18,19] In contrast, intermetallic Pt−M catalysts incorporating more acid-resistant non-noble transition metals (M = V, Cr, Zr, Nb, etc.) have received limited attention. Compared with commonly reported Pt-based alloy systems, the PtV intermetallic alloy exhibits the lowest metal dissolution, outperforming PtCo, PtMn, and PtZn systems with comparable chemical composition, structure, and morphology, highlighting the superior antidissolution capability of V among the 3d transition metals.[20] Despite their prospect of improved stability, their solid-state chemistry and long-term electrochemical performance have remained largely unexplored.[21−26] This is due to the major challenge that lies in the synthesis of these ordered intermetallic alloy nanoparticles, namely, the required high annealing temperatures for extended periods of time, which often induce severe nanoparticle sintering, resulting in a reduction in electrochemically active surface

Received: February 20, 2026
Accepted: March 12, 2026
Published: March 27, 2026

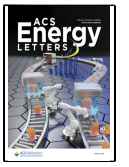

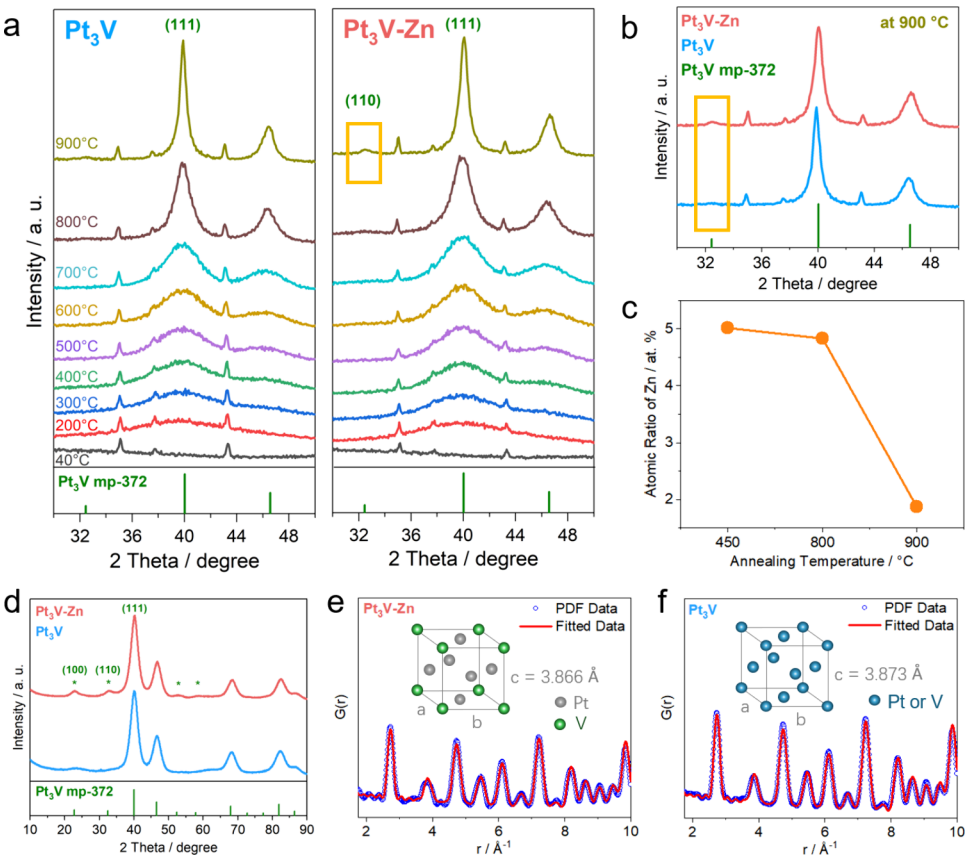

Figure 1. Synthetic strategy, structural evolution and phase transition analysis. (a) *In situ* HT-XRD in a H_2/Ar atmosphere for Pt_3V and Zn-doped Pt_3V samples. (b) XRD patterns at 900 °C. Note that the diffraction peaks at ca. 35°, 37.6°, and 43° belong to the Al_2O_3 sample holder. (c) ICP-MS results of the remaining Zn amount in the Zn-doped Pt_3V samples after annealing at 450, 800, and 900 °C, respectively. (d) *Ex situ* XRD patterns of as-annealed samples after tube furnace annealing for 1 h at 900 °C in a 4% H_2/Ar atmosphere, with the reference pattern of ordered Pt_3V from the powder diffraction file (Pt_3V mp-372) for comparison.[28] (e, f) Pair distribution function (PDF) pattern fitting of synchrotron-based WAXS measurements and the resulting lattice parameters for the leached and postannealed Pt_3V-Zn and Pt_3V, respectively.

area (ECSA).[27] New chemical strategies addressing the synthetic challenges of these intermetallics are critical to advancing durable and high-performance cathode catalysts suitable for next-generation HDV fuel cell applications.

In this study, we report a novel synthetic lattice-vacancy-mediated concept to induce disorder-to-order phase transitions in metal alloy nanoparticles for the preparation of highly ordered and durable intermetallic alloy nanoparticle catalysts. We exemplify our synthetic concept by addressing the longstanding challenge of synthesizing ordered $L1_2$-Pt_3V intermetallic nanoparticles at technologically relevant metal loadings of 50 wt % for use as hydrogen PEMFC cathodes catalyzing the ORR:

$$O_2 + 4H^+ + 4e^- \rightarrow 2H_2O$$

Our synthetic concept utilizes *cataloreactive* Zn atoms as coalloying atomic lattice dopants that evaporate under the synthesis conditions, leaving behind *in situ*-generated lattice vacancies, thereby triggering the rapid structural ordering of Pt and V atoms. In this process, the evaporated metal Zn atoms leave the resulting ordered lattice, condense, and can be reused. We demonstrate that this process yields previously elusive, high-weight-loaded, ordered $L1_2$-Pt_3V intermetallic nanoparticles that catalyze the electrochemical ORR with superior stability and performance compared to the disordered Pt_3V reference catalyst. To understand the functional role of Zn atoms in the ordering process, we applied a number of different *in situ* analysis techniques. Tracing the crystal structure evolution using *in situ* high-temperature X-ray diffraction (*in situ* HT-XRD), we succeeded in the design of an effective annealing protocol for the formation of a well-defined Zn-doped $L1_2$-Pt_3V catalyst structure characterized by superlattice reflection and a contracted lattice, which was confirmed by *ex situ* XRD and synchrotron-based wide-angle X-ray scattering (WAXS) measurements. High-angle annular dark-field scanning transmission electron microscopy (HAADF-STEM) showed a consistent atomic arrangement of the intermetallic phase of the doped $L1_2$-Pt_3V catalyst with the scattering experiments. Thanks to the Zn-vacancy-mediated structural ordering, the $L1_2$-Pt_3V catalyst exhibited a significant enhancement in both ORR catalytic activity and electrochemical stability in rotating disk electrode (RDE) setups and realistic membrane electrode assembly (MEA)-based PEMFC environments compared to the disordered A1-Pt_3V reference catalyst. Advanced characterizations, such as online inductively coupled plasma mass spectrometry (ICP-MS) and *in situ* X-ray absorption spectroscopy (XAS), demonstrated a favorable suppression in V ion leaching from the intermetallic $L1_2$-Pt_3V catalyst compared to that of its disordered counterpart. From our spectroscopic analysis, we derive two distinctly different degradation mechanisms, namely, *isotropic* V leaching and *anisotropic* cluster leaching

https://doi.org/10.1021/acsenergylett.6c00542
ACS Energy Lett. 2026, 11, 3642−3650

for the $L1_2$-Pt_3V-Zn and A1-Pt_3V catalysts, respectively, rationalizing the enhanced stability.

Carbon-supported Zn-doped intermetallic, ordered $L1_2$-Pt_3V alloy nanoparticles (henceforth denoted as $L1_2$-Pt_3V-Zn even after complete removal of Zn) and nondoped reference disordered A1-Pt_3V alloy nanoparticles were prepared by a coimpregnation route. For the $L1_2$-Pt_3V-Zn sample, the Pt, V, and Zn (initially at a 5 mol % level) precursors were stoichiometrically mixed with the carbon support in deionized water under magnetic stirring overnight, and then the mixture was dried by rotary evaporation. The non-Zn-doped disordered face-centered cubic A1-Pt_3V reference sample (space group $Fm\bar{3}m$) was prepared using the same synthesis procedure as for the Zn-doped intermetallic $L1_2$-Pt_3V-Zn sample (space group $Pm\bar{3}m$), except that only Pt and V precursors were employed. The dried powders were subsequently annealed under 4% H_2/Ar for 1 h at 900 °C, a temperature optimized by the *in situ* HT-XRD measurement. To establish a Pt-rich core−shell alloy particle structure, both as-annealed samples were leached in 0.5 M H_2SO_4 at 80 °C for 24 h, followed by mild postannealing at 400 °C for 2 h under 4% H_2/Ar. This resulted in the complete removal of Zn for the $L1_2$-Pt_3V-Zn sample.

To monitor the crystalline structural evolution of Pt_3V lattices during thermal treatment and , more specifically, to comparatively track disorder-to-order phase transitions, *in situ* HT-XRD analysis of the two metal alloy samples, Pt_3V-Zn and Pt_3V, was used. Figure 1a compares the diffraction patterns of the Pt_3V-Zn and Pt_3V samples recorded at temperatures between 40 and 900 °C. The initial scan at 40 °C showed no discernible diffraction peaks from Pt- or V-based crystalline phases, indicating the amorphous or highly dispersed nature of the metal precursors. Upon reaching 200 °C, the emergence of a broad (111) reflection at ca. 40.2° indicated the nucleation of nanocrystalline Pt_3V alloy nanoparticles. As the temperature increased from 200 to 900 °C, the (111) peak progressively sharpened, suggesting an increase in crystallite size for both samples.

Unlike the undoped sample, the Zn-doped Pt_3V-Zn sample exhibited a clear disorder-to-order phase transition to the elusive ordered intermetallic Pt_3V phase, as evidenced by the appearance of a (110) superlattice peak at ca. 32.8° (yellow box), characteristic of the $L1_2$ intermetallic lattice structure. Furthermore, the (111) peak of the Pt_3V-Zn sample shifted toward larger 2θ values compared to its undoped counterpart, indicating a higher degree of alloying and associated lattice contraction, facilitated by Zn incorporation into the lattice (Figure 1b). Given the significantly lower melting and evaporation points of Zn relative to Pt and V, its thermal stability during annealing was assessed using *ex situ* ICP-MS. As shown in Figure 1c, the Zn content remained close to the nominal synthesis ratio after 450 and 800 °C annealing; however, it dropped sharply upon 900 °C annealing, suggesting substantial Zn evaporation. We propose that the Zn volatilization at elevated temperatures might introduce lattice vacancies that enhance V atom mobility,[29] thereby promoting both alloying and structural ordering within the cubic Pt−V matrix. The compositions of the final catalysts (after acid leaching and postannealing) were determined by *ex situ* ICP-MS (Table S1) and confirmed high Pt loadings of ca. 50 wt % in both samples combined with complete removal of Zn from the $L1_2$-Pt_3V-Zn sample.

Guided by the small-batch *in situ* HT-XRD results, the annealing temperature of 900 °C was selected to synthesize larger batches of ordered $L1_2$-Pt_3V-Zn and disordered A1-Pt_3V catalysts. The *ex situ* XRD pattern (Figure 1d) of $L1_2$-Pt_3V-Zn exhibited characteristic (100) and (110) superlattice peaks that are absent in the disordered counterpart. Pair distribution function (PDF) analysis (Figure 1e,f) confirmed the cubic-type structures (primitive and face-centered) for the two catalysts. Notably, $L1_2$-Pt_3V-Zn exhibits a smaller lattice parameter (3.866 Å) than A1-Pt_3V (3.873 Å), suggesting lattice contraction in the ordered phase. This contraction is expected to alter the electronic structure and oxygen binding energy of surface Pt sites, contributing to the enhanced ORR activity discussed in the following electrochemical analysis.

To further visualize the successful formation of the intermetallic $L1_2$ phase in the presence of Zn doping, high-resolution STEM coupled with energy-dispersive X-ray spectroscopy (EDX) and HAADF imaging was performed. As shown in Figure 2a, STEM-EDX elemental mapping

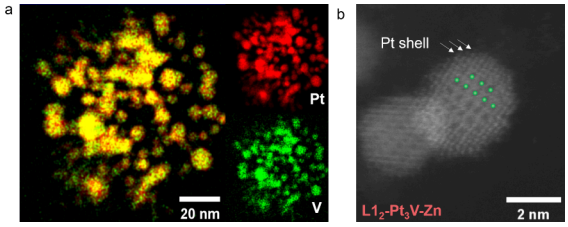

Figure 2. Microscopic and compositional analysis. (a) STEM-EDX mapping of the leached and postannealed intermetallic $L1_2$-Pt_3V-Zn sample with Pt (red) and V (green) elements. (b) HAADF-STEM image with the atomic arrangement of $L1_2$-Pt_3V-Zn marked by arrows for the Pt shell and green dots for V atoms.

demonstrates a uniform distribution of Pt and V across the nanoparticle matrix. The HAADF-STEM image in Figure 2b reveals the characteristic atomic-scale ordering of the $L1_2$-Pt_3V crystal with ca. 3 layers of Pt shell, consistent with the expected structure after acid leaching and postannealing. The STEM images (Figures S1 and S2) confirm a narrow particle size distribution for both the acid-leached $L1_2$-Pt_3V-Zn catalyst and the acid-leached disordered A1-Pt_3V catalyst, with similar average sizes of 3.51 ± 0.8 and 3.55 ± 0.9 nm, respectively. These values closely match the crystallite sizes derived from XRD analysis using the Scherrer equation (Table S2).[30,31]

The ORR activity and stability of the ordered $L1_2$-Pt_3V-Zn and disordered A1-Pt_3V catalysts were first evaluated using electrochemical cyclic voltammetry (CV), surface-adsorbed CO stripping to quantify electrochemical surface areas, and linear sweep voltammetry (LSV), all techniques applied in a three-electrode liquid electrolyte RDE setup. The CVs recorded in N_2-saturated 0.1 M $HClO_4$ electrolyte (Figure 3a) were used to determine the ECSA values via hydrogen underpotential deposition ($ECSA_{Hupd}$), resulting in values of 60.5 and 60 $m^2\ g_{Pt}^{-1}$ for $L1_2$-Pt_3V-Zn and A1-Pt_3V, respectively (Table S3). The ECSA values from CO stripping ($ECSA_{CO}$) were 73.1 and 65.8 $m^2\ g_{Pt}^{-1}$ for the ordered and disordered catalysts, respectively, consistent with the small difference in the mean particle size. Notably, the ratio of $ECSA_{CO}/ECSA_{Hupd}$ was significantly higher for the $L1_2$-Pt_3V-Zn catalyst, which is a direct consequence of a lower surface coverage of adsorbed H atoms on the ordered catalysts. This effect is known to be caused by lower H chemisorption on

https://doi.org/10.1021/acsenergylett.6c00542
ACS Energy Lett. 2026, 11, 3642−3650

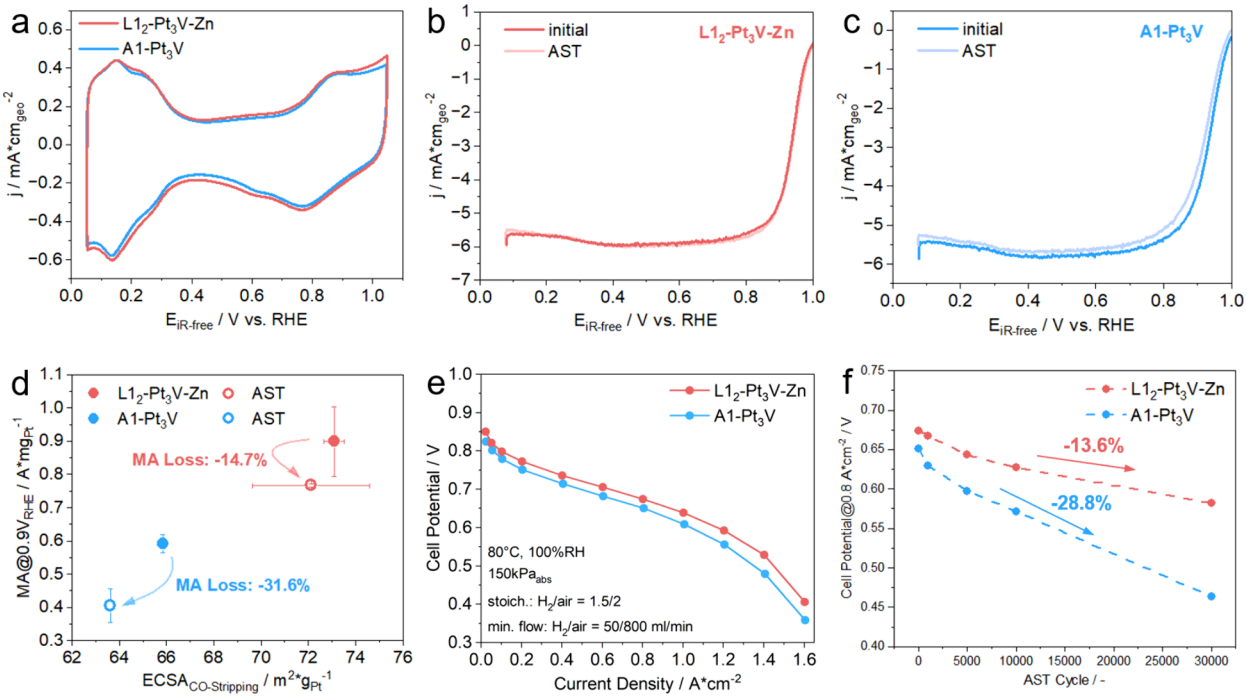

Figure 3. Electrochemical evaluation of the ordered and disordered Pt_3V catalysts. (a–d) RDE measurements for ordered $L1_2$-Pt_3V-Zn (red) and disordered A1-Pt_3V (blue): (a) Cyclic voltammetry (CV) curves in N_2-saturated 0.1 M $HClO_4$ electrolyte at room temperature with a scan rate of 20 mV s^{-1}; (b, c) linear sweep voltammetry (LSV) curves with a scan rate of 20 mV s^{-1} under a rotating rate of 1600 rpm before and after 30,000 cycles of a trapezoidal-wave accelerated stress test (AST) by holding for 3 s at 0.6 and 0.95 V_{RHE} each with a scan rate of 750 mV s^{-1} between potentials; (d) ECSA from the CO-stripping method and MA at 0.9 V_{RHE} before and after AST. (e, f) MEA single cell tests: (e) MEA ORR polarization curves collected under the conditions noted in the graph; (f) cell potential evolution during AST, consisting of 30,000 square-wave AST by holding potentials at 0.6 and 0.95 V with a dwell time of 3 s.

compressed Pt surfaces of contracted Pt alloy bulk lattices,[32−34] as supported by our synchrotron-based WAXS/PDF results from Figure 1. Subsurface V atoms modify the surface electronic structure of Pt, diminishing hydrogen adsorption while preserving CO binding.[35] To analyze the electrochemical stability of the two Pt_3V catalysts after an accelerated stress test (AST), CVs in N_2-saturated environment and CO-stripping analyses were performed before and after 30,000 potential cycles for the $L1_2$-Pt_3V-Zn and A1-Pt_3V catalysts (Figures S3 and S4, respectively). The overlapping voltammetric profiles of the $L1_2$-Pt_3V-Zn evidenced excellent tolerance to chemical leaching of V, while the anodic stripping peak shift of the A1-Pt_3V catalyst in Figure S4 suggests subsurface V dealloying and the creation of a thicker Pt overlayers.[35]

Figure 3b,c compares the catalytic ORR activities before and after the 30,000-cycle AST of the two catalyst systems. In line with our voltammetric analysis, the $L1_2$-Pt_3V-Zn catalyst exhibited minimal catalytic performance degradation, whereas the A1-Pt_3V sample suffered a noticeable negative shift in the half-wave potential ($E_{1/2}$), indicative of substantial catalytic ORR activity loss. We attribute this catalytic activity loss to the previously identified subsurface V leaching during the electrochemical tests.

Correlation plots relating mass-specific catalytic ORR activities (MA) at 0.9 V versus the reversible hydrogen electrode (V_{RHE}) and CO-stripping-derived electrochemical surface areas ($ECSA_{CO}$) are reported in Figure 3d, with the ordered catalyst achieving a significantly higher MA of 0.9 A mg_{Pt}^{-1}, compared to 0.59 A mg_{Pt}^{-1} for its disordered counterpart at more favorable surface areas. The catalytic performance stability of the $L1_2$-Pt_3V-Zn catalyst was markedly superior to that of A1-Pt_3V. The $L1_2$-Pt_3V-Zn catalyst shows superior retention of activity after 30,000 AST cycles, with only a 14.7% decrease in MA, compared to a 31.6% loss for A1-Pt_3V. Considering that the two catalysts have comparable nanoparticle sizes, this improvement is attributed to the structural ordering and associated lattice contraction in the $L1_2$ phase, which modulates the Pt−O binding energy to favor optimal ORR kinetics and inhibits V leaching by stabilizing its position in the lattice.[32,36]

Next, the $L1_2$-Pt_3V-Zn and A1-Pt_3V catalysts were cast into cathode layers of MEAs that were deployed in a realistic single hydrogen/air PEM fuel cell assembly, and their electrochemical ORR performance was investigated. Figure 3e reports the fuel cell polarization performance curves up to applied current densities of 1.6 A cm^{-2}. The ordered $L1_2$-Pt_3V-Zn electrode revealed superior cell performance across the entire load range, including the kinetic, ohmic, and transport-limited regimes. The kinetic mass activity at 0.9 V cell voltage, while not optimized, surpassed that of the disordered alloy by a factor of 10. Noteworthy are the enhanced cell voltages in the transport-limited region that can point to less V ion leaching into the proton-conducting ionomer in the catalyst layer (see direct evidence below). Notably, after 30,000 cycles of square-wave AST, the $L1_2$-Pt_3V-Zn catalyst exhibited markedly higher cell voltage durability, with a 13.6% voltage loss at 0.8 A cm^{-2}, in contrast to a 28.8% voltage loss for the A1-Pt_3V catalyst (Figure 3f). We associate the enhancements in activity and durability observed in both liquid-cell RDE and single-cell MEA with the critical role of atomic ordering in the intermetallic $L1_2$-Pt_3V-Zn system that results in reduced V

https://doi.org/10.1021/acsenergylett.6c00542
ACS Energy Lett. 2026, 11, 3642−3650

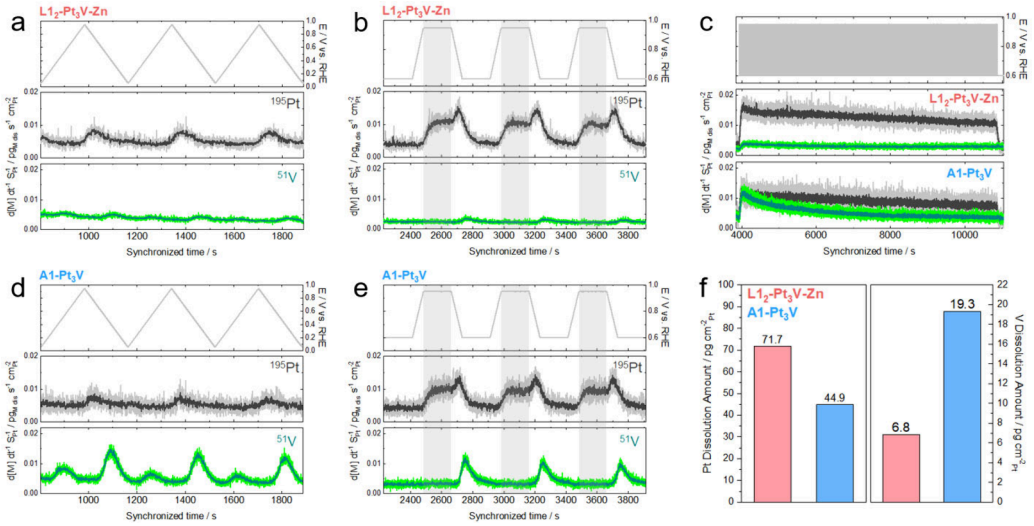

Figure 4. Metal dissolution behavior analysis. Online ICP-MS measurements for (a, b) intermetallic L1$_2$-Pt$_3$V-Zn and (d, e) disordered A1-Pt$_3$V: (a, d) CV-based potential cycling from 0.05 to 0.95 V_{RHE} with a scan rate of 5 mV s^{-1}; (b, e) trapezoidal-wave cycling by holding potentials at 0.6 and 0.95 V_{RHE} each for 3 min with a scan rate of 5 mV s^{-1}. (c, f) Accumulated dissolution amounts of Pt and V after 1000 cycles of trapezoidal-wave AST by holding for 3 s at 0.6 and 0.95 V_{RHE} each with a scan rate of 750 mV s^{-1} between potentials.

ion leaching and ionomer poisoning during fuel cell operation. In order to support this hypothesis, we further examined and compared our two alloy systems using online ICP-MS and *in situ* XAS studies, as described below.

To gain deeper insight into the enhanced electrochemical stability of the intermetallic L1$_2$-Pt$_3$V-Zn catalyst during ORR, online ICP-MS was employed to monitor the time- and potential-resolved dissolution of Pt and V in 0.1 M $HClO_4$ at 25 °C. The electrochemical protocol for the online ICP-MS measurements is shown in Figure S5. As shown in Figure 4a,d, during three consecutive triangle-wave CV cycles from 0.05 to 0.95 V_{RHE}, the ordered and disordered Pt$_3$V catalysts present similar dissolution trends but with different intensities. First, Pt dissolution peaks appear prominently in the cathodic scan, while V dissolves during both anodic and cathodic scans. The cathodic Pt dissolution is attributed to the place-exchange mechanism,[37−39] wherein surface oxygen atoms exchange their location with Pt atoms during anodic scans to get into subsurface positions, resulting in a cathodic surface Pt dissolution peak; this is consistent with prior reports on Pt-based alloys containing less-noble metals such as Cu, Co, and rare-earth elements.[40−42] In the case of V dissolution, distinct anodic and cathodic peaks are observed at ca. 0.3 V_{RHE} (surface oxidation) and 0.4 V_{RHE} (surface reduction), respectively. Based on the thermodynamic prediction given by the Pourbaix diagram,[43] the anodic dissolution event could be linked to the oxidation of metallic V^0 to V^{3+}, while the cathodic dissolution likely corresponds to the reduction of VO^{2+} to V^{3+}. Interestingly, A1-Pt$_3$V (Figure 4d) exhibited a significantly larger specific V dissolution rate compared to its ordered L1$_2$ counterpart (Figure 4a), suggesting that structural lattice ordering enhances the chemical stability of V.

This trend was further observed in the AST-like potential-hold measurements (Figure 4b,e), where the potentials were held at 0.6 and 0.95 V_{RHE} for 3 min; clearly, no V anodic dissolution was observed. This feature is in line with the Pourbaix diagram, since it is expected that V^{3+} is absent within 0.6 and 0.95 V_{RHE}. When the potential was held at 0.95 V_{RHE}, the Pt dissolution rate initially increased and then reached a stationary plateau. This behavior aligns with the dissolution of low-coordinated sites and formation/dissolution of amorphous oxides and metastable phases, until stable Pt oxide layers are established.[44] The resulting surface passivation accompanied by the formation of subsurface oxides weakens Pt−Pt bonds. This bond weakening facilitates cathodic Pt dissolution through surface detachment processes,[45] as evidenced by a pronounced cathodic Pt dissolution peak.

To quantify the specific metal dissolution of both catalysts under the identical AST protocol used in the RDE experiments, 1000 potential cycles were applied. The specific dissolution profiles in Figure 4c show an initial spike followed by gradual passivation over the AST.

While the ordered L1$_2$-Pt$_3$V-Zn exhibited Pt dissolution trajectories comparable to its counterpart (Figure 4f), its V dissolution is nearly 2 times lower than that of A1-Pt$_3$V. This reduces V cation poisoning of the cathode layer ionomer and can account for the enhanced PEM cell stability. As the two catalysts possessed comparable particle sizes, compositions, and core−shell structures following the identical synthesis, acid leaching, and postannealing treatment, we attribute the distinct V stability largely to an effect by the ordered alloy lattice. The presence of dissolving VO_x species at the surface of the disordered A1-Pt$_3$V catalysts appears to slow surface Pt atom dissolution somewhat (Figure 4f), as previously observed on L1$_2$-Pt$_3$Cr and L1$_0$-PtCr intermetallics.[22] However, the excess of such VO_x species can partially block the Pt atoms at the surface, lowering the ECSA, consistent with the RDE results. With regard to the reduced V dissolution in the L1$_2$-Pt$_3$V-Zn sample, the intermetallic core can more efficiently stabilize V atoms within the particle. This structure feature could probably limit the direct exposure of V to the acidic electrolyte while increasing the exposure of Pt at the surface. As a result, the L1$_2$-Pt$_3$V-Zn sample exhibited higher Pt dissolution than the A1-Pt$_3$V sample.

To elucidate the origin of enhanced stability conferred by structural ordering and to probe the degradation mechanisms of the ordered and disordered Pt$_3$V catalysts, *in situ* XAS measurements were performed at the Pt L$_3$-edge. The

https://doi.org/10.1021/acsenergylett.6c00542
ACS Energy Lett. 2026, 11, 3642−3650

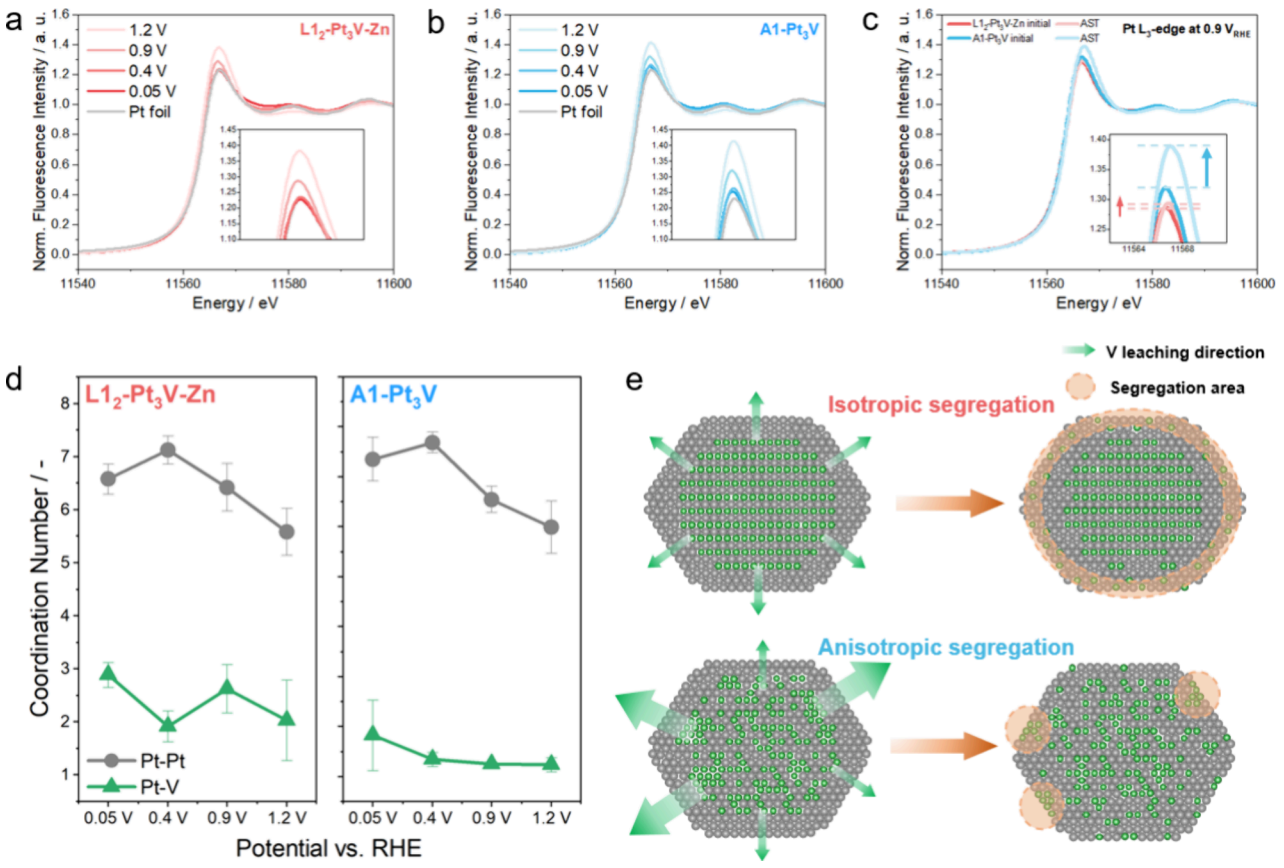

Figure 5. Structural stability and degradation mechanism investigation. (a–c) *In situ* XAS measurements: (a, b) spectra collected by holding the samples at different potentials before AST (initial) for $L1_2$-Pt_3V-Zn and A1-Pt_3V, respectively; (c) spectra at 0.9 V_{RHE} before and after 5000 cycles of a trapezoidal-wave AST. (d) Coordination numbers from Fourier transform EXAFS-fitting. (e) Illustrations of V leaching behavior for the ordered (upper) and disordered (lower) catalysts.

experiments were conducted in a validated *in situ* half-cell by holding potentials at 0.05, 0.4, 0.9, and 1.2 V_{RHE} before and after AST.[46] Figure 5a,b displays the potential-dependent X-ray absorption near-edge structure (XANES) spectra for the $L1_2$-Pt_3V-Zn and A1-Pt_3V catalysts, respectively, with Pt foil used as a reference. The insets emphasize changes in the white-line intensity, which is indicative of the density of unoccupied Pt 5d states and hence correlates with the oxidation state of Pt.[19,47] As expected, increasing the applied potential results in an increase in the white-line intensity for both catalysts, but with different magnitudes.

At 0.05 V_{RHE}, the $L1_2$-Pt_3V-Zn catalyst exhibits a white-line intensity nearly overlapping that of the Pt foil, implying a Pt oxidation state close to metallic. In contrast, at this potential, A1-Pt_3V shows a significantly higher white-line intensity, suggesting an elevated oxidation state. Figure 5c compares the XANES spectra at 0.9 V_{RHE} before and after AST. The increase in the white-line intensity and a positive energy shift of the peak after AST are indicative of catalyst aging, likely by V dealloying, resulting in a higher average oxidation state of Pt. Strikingly, the relative increase in the white-line intensity of the $L1_2$-Pt_3V-Zn catalyst was only 0.5%, significantly lower than the 5.3% increase observed for the disordered A1-Pt_3V catalyst. This marked difference confirms that the ordered catalyst possesses a much higher oxidation resistance, consistent with the electrochemical performance and online ICP-MS findings. The attenuated V leaching in the intermetallic structure helps preserve Pt electronic properties by maintaining electron donation from V, thus protecting Pt against oxidative degradation. In contrast, extensive V dealloying in the disordered sample disrupts this electron transfer, leaving Pt more susceptible to oxidation.

To further understand the structural dynamics, coordination numbers were extracted by fitting the extended X-ray absorption fine structure (EXAFS) spectra at various potentials (Figure 5d). In all potentials, $L1_2$-Pt_3V-Zn consistently displays lower Pt–Pt coordination numbers and larger Pt–V coordination numbers compared to A1-Pt_3V, affirming a higher degree of structural ordering, in agreement with the XRD and WAXS results. Upon increasing the potential, the Pt–V coordination numbers generally decreased due to V dealloying. However, an unexpected trend was observed for $L1_2$-Pt_3V-Zn as the potential was increased from 0.4 to 0.9 V_{RHE}, in that the Pt–V coordination number increased. This behavior suggests that under moderately oxidative conditions, the V atoms preferentially migrate from the core to the surface, increasing their proximity to Pt at the (near) surface. This redistribution enhances Pt–V coordination at the (near) surface, which is a phenomenon absent in the disordered catalyst.

Based on these observations, we propose a structural model for the degradation mechanisms for V leaching in the ordered and disordered catalysts (Figure 5e). In the ordered $L1_2$ crystal, V atoms undergo *isotropic* segregation/leaching, uniformly migrating toward the surface and resulting in evenly dispersed Pt–V coordination at the (near) surface. In contrast,

https://doi.org/10.1021/acsenergylett.6c00542
ACS Energy Lett. 2026, 11, 3642–3650

the disordered A1 crystal undergoes *anisotropic* clustered V migration, leading to heterogeneous V segregation and a lower average Pt−V coordination. Overall, these *in situ* XAS results underscore the critical role of intermetallic ordering in stabilizing the non-noble atoms such as V in the present Pt alloy catalysts. The ability of the ordered phase to sustain Pt−V bonding under oxidative conditions directly translates to enhanced oxidation resistance, reduced degradation, and superior long-term ORR durability.

In this work, we present a new robust synthetic approach for preparing otherwise elusive structurally ordered intermetallics. The synthetic route utilizes *in situ*-generated lattice vacancies introduced by evaporating Zn atoms as a *cataloreactant*. We demonstrated our approach in the preparation of an acid-stable $L1_2$-Pt_3V nanocatalyst with an unprecedented high loading of ca. 50 wt % Pt. *In situ* HT-XRD measurements were employed to monitor and clarify the structural transformation of the ordered lattice during annealing. Complementary *ex situ* XRD and synchrotron-based WAXS confirmed the Zn-assisted phase transition and the formation of a superlattice characteristic of the $L1_2$ phase, distinctly differentiating it from the disordered A1-Pt_3V counterpart. High-resolution HAADF-STEM imaging further revealed the atomically ordered arrangement within the $L1_2$-Pt_3V-Zn crystal.

The ordered electrocatalyst material demonstrated substantially enhanced ORR activity and acid-leaching stability in both RDE and MEA tests, underscoring the advantages conferred by the intermetallic structure. Online ICP-MS measurements revealed suppressed V dissolution in the intermetallic $L1_2$ phase, attributing its superior electrochemical stability to intrinsic structural ordering. Furthermore, the *in situ* XAS measurements unraveled distinct degradation pathways. The ordered catalyst exhibited *isotropic* V segregation, which maintained Pt−V coordination at the (near) surface, while the disordered catalyst underwent *anisotropic* clusterwise V leaching, leading to accelerated degradation and dealloying.

Overall, this study highlights the effectiveness of our *in situ* lattice-vacancy-mediated formation of stable ordered intermetallic nanocatalysts, effectively overcoming the synthetic challenges of ordered Pt alloy systems. The insights gained into structure−stability−performance relationships provide a valuable framework for the rational design of ultradurable high-performance ORR catalysts in PEMFCs.

■ ASSOCIATED CONTENT

Supporting Information

The Supporting Information is available free of charge at https://pubs.acs.org/doi/10.1021/acsenergylett.6c00542.

STEM images and size distributions, CV under N_2 and CO environments in RDE with AST, protocol for online ICP-MS measurements, EXAFS fitting results, ICP-MS sample compositions, TEM particle sizes and XRD crystallite sizes, and ECSA and MA before and after AST in RDE (PDF)

■ AUTHOR INFORMATION

Corresponding Author

Peter Strasser − *Department of Chemistry, Chemical Engineering Division, Technical University of Berlin, 10623 Berlin, Germany;* orcid.org/0000-0002-3884-436X; Email: pstrasser@tu-berlin.de

Authors

Jiasheng Lu − *Department of Chemistry, Chemical Engineering Division, Technical University of Berlin, 10623 Berlin, Germany*

Carlos A. Campos-Roldán − *ICGM, Univ. Montpellier, CNRS, ENSCM, 34095 Montpellier, France;* orcid.org/0000-0002-1517-9037

Thomas Merzdorf − *Department of Chemistry, Chemical Engineering Division, Technical University of Berlin, 10623 Berlin, Germany*

Xingli Wang − *Department of Chemistry, Chemical Engineering Division, Technical University of Berlin, 10623 Berlin, Germany;* orcid.org/0000-0003-2785-9707

Lujin Pan − *Department of Chemistry, Chemical Engineering Division, Technical University of Berlin, 10623 Berlin, Germany*

Hong Nhan Nong − *Department of Chemistry, Chemical Engineering Division, Technical University of Berlin, 10623 Berlin, Germany*

Frederik Firschke − *Department of Chemistry, Chemical Engineering Division, Technical University of Berlin, 10623 Berlin, Germany*

Sören Selve − *Center for Electron Microscopy (ZELMI), Technische Universität Berlin, 10623 Berlin, Germany*

Jakub Drnec − *European Synchrotron Radiation Facility (ESRF), 38000 Grenoble, France*

Deborah Jones − *ICGM, Univ. Montpellier, CNRS, ENSCM, 34095 Montpellier, France*

Fabio Dionigi − *Department of Chemistry, Chemical Engineering Division, Technical University of Berlin, 10623 Berlin, Germany;* orcid.org/0000-0002-0576-024X

Complete contact information is available at: https://pubs.acs.org/10.1021/acsenergylett.6c00542

Author Contributions

J.L. and P.S. conceived the project. J.L. synthesized all the samples and carried out the *in situ* HT-XRD measurements, *ex situ* XRD, RDE electrochemical measurements, and data analysis. C.A.C.R. performed the online ICP-MS measurements and data analysis. T.M. and J.L. conducted the MEA measurements. S.S. and X.W. contributed to STEM/TEM measurements. H.N.N. and J.L. carried out *in situ* XAS measurements and data analysis. F.F. conducted *ex situ* ICP-MS measurements. J.D. carried out the synchrotron-based WAXS measurements and their PDF analysis. P.S. provided guidance and constructive ideas throughout this project to ensure its successful outcome. All authors contributed to the discussion part, drew conclusions, and participated in revising and finalizing the text and figures.

Notes

The authors declare no competing financial interest.

■ ACKNOWLEDGMENTS

We thank the HIGHLANDER Project supported by the Clean Hydrogen Partnership and its members Hydrogen Europe and Hydrogen Europe Research under Grant Agreement 101101346. We thank the Deutsche Forschungsgemeinschaft (German Research Foundation, DFG) for financial support under Grant STR-596/21-1. We thank the Zentraleinrichtung Elektronenmikroskopie (ZELMI) at Technische Universität Berlin (TUB) in the context of the Alliance Center Electron

Microscopy (ACEM) funded under the Excellence Strategy of the Federal Government and the Länder by the Berlin University Alliance (BUA) for support in TEM measurements. We thank synchrotron SOLEIL for the provision of synchrotron radiation beamtime at the ROCK beamline via Proposal 20231730, and we thank Dr. Stéphanie Belin for her support. This work was supported by a public grant overseen by the French National Research Agency (ANR) as part of the "Investissements d'Avenir" Program (reference: ANR-10-EQPX-45). We thank the ID31 beamline in the European Synchrotron Radiation Facility (ESRF) for the high-throughput WAXS measurements (DOI: 10.15151/ESRF-ES-1965480968). We thank Astrid Müller-Klauke from TUB for the *ex situ* ICP-MS.

REFERENCES

(1) Debe, M. K. Electrocatalyst approaches and challenges for automotive fuel cells. *Nature* **2012**, *486*, 43−51.
(2) Gasteiger, H. A.; Kocha, S. S.; Sompalli, B.; Wagner, F. T. Activity benchmarks and requirements for Pt, Pt-alloy, and non-Pt oxygen reduction catalysts for PEMFCs. *Appl. Catal., B* **2005**, *56*, 9−35.
(3) Turner, J. A. Sustainable Hydrogen Production. *Science* **2004**, *305*, 972−974.
(4) Cullen, D. A.; et al. New roads and challenges for fuel cells in heavy-duty transportation. *Nat. Energy* **2021**, *6*, 462−474.
(5) Cao, X.; et al. Sandwiching intermetallic Pt_3Fe and ionomer with porous N-doped carbon layers for oxygen reduction reaction. *Nat. Commun.* **2025**, *16*, 2851.
(6) Yang, C.-L.; et al. Sulfur-anchoring synthesis of platinum intermetallic nanoparticle catalysts for fuel cells. *Science* **2021**, *374*, 459−464.
(7) Li, J.; et al. Hard-Magnet $L1_0$-CoPt Nanoparticles Advance Fuel Cell Catalysis. *Joule* **2019**, *3*, 124−135.
(8) Song, T.-W.; et al. Small molecule-assisted synthesis of carbon supported platinum intermetallic fuel cell catalysts. *Nat. Commun.* **2022**, *13*, 6521.
(9) Zeng, Y.; et al. Regulating Catalytic Properties and Thermal Stability of Pt and PtCo Intermetallic Fuel-Cell Catalysts via Strong Coupling Effects between Single-Metal Site-Rich Carbon and Pt. *J. Am. Chem. Soc.* **2023**, *145*, 17643−17655.
(10) Pan, L.; et al. From Seeds to Cell: Improving PEMFC Performance and Durability by Seed-Mediation Synthesis for PtNiIr ORR Nanocatalysts. *Adv. Sci.* **2025**, *12*, e05958.
(11) Pan, L.; et al. Enhancing the Performance of Shape-Controlled Octahedral Rhodium-Doped PtNi Nanoalloys inside Hydrogen−Air Fuel Cell Cathodes Using a Rational Design of Catalysts, Supports, and Layering. *ACS Catal.* **2024**, *14*, 10−20.
(12) Đukić, T.; et al. Understanding the Crucial Significance of the Temperature and Potential Window on the Stability of Carbon Supported Pt-Alloy Nanoparticles as Oxygen Reduction Reaction Electrocatalysts. *ACS Catal.* **2022**, *12*, 101−115.
(13) Wang, X.; et al. Effect of Particle Size on the Dissolution of Pt_3Co/C and Pt/C PEMFC Electrocatalysts. *J. Electrochem. Soc.* **2021**, *168*, 054516.
(14) Ramaswamy, N.; et al. Mitigation of PtCo/C Cathode Catalyst Degradation via Control of Relative Humidity. *J. Electrochem. Soc.* **2021**, *168*, 124512.
(15) Jia, Q.; et al. Circumventing Metal Dissolution Induced Degradation of Pt-Alloy Catalysts in Proton Exchange Membrane Fuel Cells: Revealing the Asymmetric Volcano Nature of Redox Catalysis. *ACS Catal.* **2016**, *6*, 928−938.
(16) Cui, C.; Gan, L.; Heggen, M.; Rudi, S.; Strasser, P. Compositional segregation in shaped Pt alloy nanoparticles and their structural behaviour during electrocatalysis. *Nat. Mater.* **2013**, *12*, 765−771.
(17) Koh, S.; Strasser, P. Electrocatalysis on Bimetallic Surfaces: Modifying Catalytic Reactivity for Oxygen Reduction by Voltammetric Surface Dealloying. *J. Am. Chem. Soc.* **2007**, *129*, 12624−12625.
(18) Liang, J.; et al. Metal bond strength regulation enables large-scale synthesis of intermetallic nanocrystals for practical fuel cells. *Nat. Mater.* **2024**, *23*, 1259−1267.
(19) Liu, X.; et al. Introducing Electron Buffers into Intermetallic Pt Alloys against Surface Polarization for High-Performing Fuel Cells. *J. Am. Chem. Soc.* **2024**, *146*, 2033−2042.
(20) Campos-Roldán, C. A.; et al. Dissolution Trends of Platinum-Based Intermetallic Nanocatalysts toward the Acidic Oxygen Reduction Reaction. *ACS Catal.* **2025**, *15*, 17950−17957.
(21) Ramaswamy, N.; Kongkanand, A.; Wortman, J.; Gu, W. Review—Meeting Fuel Cell Catalyst Requirements for Heavy-Duty Vehicle Applications. *J. Electrochem. Soc.* **2025**, *172*, 024501.
(22) Campos-Roldán, C. A.; et al. Mitigating the Pt Dissolution of Pt−Cr Intermetallics during the Oxygen Reduction Reaction in Acid Medium. *ACS Catal.* **2025**, *15*, 14180−14190.
(23) Antolini, E.; Passos, R. R.; Ticianelli, E. A. Electrocatalysis of oxygen reduction on a carbon supported platinum−vanadium alloy in polymer electrolyte fuel cells. *Electrochim. Acta* **2002**, *48*, 263−270.
(24) Haile, A. S.; Yohannes, W.; Mekonnen, Y. S. Oxygen reduction reaction on Pt-skin $Pt_3V(111)$ fuel cell cathode: a density functional theory study. *RSC Adv.* **2020**, *10*, 27346−27356.
(25) Ramaswamy, N.; et al. Surface Decoration of Platinum Catalysts by ZrO_{2-x} Nanoclusters for Durable Fuel Cell Applications. *ACS Catal.* **2024**, *14*, 4441−4452.
(26) Yano, H.; Kataoka, M.; Yamashita, H.; Uchida, H.; Watanabe, M. Oxygen Reduction Activity of Carbon-Supported Pt−M (M = V, Ni, Cr, Co, and Fe) Alloys Prepared by Nanocapsule Method. *Langmuir* **2007**, *23*, 6438−6445.
(27) Li, J.; Sun, S. Intermetallic Nanoparticles: Synthetic Control and Their Enhanced Electrocatalysis. *Acc. Chem. Res.* **2019**, *52*, 2015−2025.
(28) *Materials Explorer: VPt_3 mp-372*. The Materials Project, 2020. https://next-gen.materialsproject.org/materials/mp-372.
(29) Wang, Z.; et al. Vacancy driven surface disorder catalyzes anisotropic evaporation of ZnO (0001) polar surface. *Nat. Commun.* **2022**, *13*, 5616.
(30) Magnussen, O. M.; et al. In Situ and Operando X-ray Scattering Methods in Electrochemistry and Electrocatalysis. *Chem. Rev.* **2024**, *124*, 629−721.
(31) Scherrer, P. In *Kolloidchemie Ein Lehrbuch*; Zsigmondy, R., Ed.; Springer: Berlin, 1912; pp 387−409.
(32) Strasser, P.; et al. Lattice-strain control of the activity in dealloyed core−shell fuel cell catalysts. *Nat. Chem.* **2010**, *2*, 454−460.
(33) Chattot, R.; et al. Electrochemical Strain Dynamics in Noble Metal Nanocatalysts. *J. Am. Chem. Soc.* **2021**, *143*, 17068−17078.
(34) *Electrochemistry*; Alkire, R. C., Kolb, D. M., Kibler, L. A., Lipkowski, J., Eds; Advances in Electrochemical Science and Engineering, Vol. *14*; Wiley-VCH, 2013. DOI: 10.1002/9783527680436.
(35) Rudi, S.; Cui, C.; Gan, L.; Strasser, P. Comparative Study of the Electrocatalytically Active Surface Areas (ECSAs) of Pt Alloy Nanoparticles Evaluated by Hupd and CO-stripping voltammetry. *Electrocatalysis* **2014**, *5*, 408−418.
(36) Stamenkovic, V.; et al. Changing the Activity of Electrocatalysts for Oxygen Reduction by Tuning the Surface Electronic Structure. *Angew. Chem., Int. Ed.* **2006**, *45*, 2897−2901.
(37) Topalov, A. A.; et al. Towards a comprehensive understanding of platinum dissolution in acidic media. *Chem. Sci.* **2014**, *5*, 631−638.
(38) Fuchs, T.; et al. Anodic and Cathodic Platinum Dissolution Processes Involve Different Oxide Species. *Angew. Chem., Int. Ed.* **2023**, *62*, e202304293.
(39) Tilak, B. V.; Conway, B. E.; Angerstein-Kozlowska, H. The real condition of oxidized pt electrodes: Part III. Kinetic theory of formation and reduction of surface oxides. *J. Electroanal. Chem. Interfacial Electrochem.* **1973**, *48*, 1−23.

(40) Campos-Roldán, C. A.; et al. Metal-oxide phase transition of platinum nanocatalyst below fuel cell open-circuit voltage. *Nat. Commun.* **2025**, *16*, 936.
(41) Gatalo, M.; et al. Comparison of Pt−Cu/C with Benchmark Pt−Co/C: Metal Dissolution and Their Surface Interactions. *ACS Appl. Energy Mater.* **2019**, *2*, 3131−3141.
(42) Campos-Roldán, C. A.; et al. Structure Dynamics of Carbon-Supported Platinum-Neodymium Nanoalloys during the Oxygen Reduction Reaction. *ACS Catal.* **2023**, *13*, 7417−7427.
(43) Povar, I.; et al. Revised Pourbaix diagrams for the vanadium − water system. *J. Electrochem. Sci. Eng.* **2019**, *9*, 75−84.
(44) Campos-Roldán, C. A.; et al. Deciphering the Atomic-Scale Degradation of Carbon-Supported Platinum−Yttrium Nanoalloys during the Oxygen Reduction Reaction in Acidic Medium. *ACS Catal.* **2024**, *14*, 11941−11948.
(45) Topalov, A. A.; et al. Dissolution of Platinum: Limits for the Deployment of Electrochemical Energy Conversion? *Angew. Chem., Int. Ed.* **2012**, *51*, 12613−12615.
(46) Frisch, M. L.; et al. Unraveling the synergistic effects of Cu-Ag tandem catalysts during electrochemical CO_2 reduction using nanofocused X-ray probes. *Nat. Commun.* **2023**, *14*, 7833.
(47) Timoshenko, J.; Roldan Cuenya, B. In Situ/Operando Electrocatalyst Characterization by X-ray Absorption Spectroscopy. *Chem. Rev.* **2021**, *121*, 882−961.

https://doi.org/10.1021/acsenergylett.6c00542
ACS Energy Lett. 2026, 11, 3642−3650